Effective model for superconductivity in magic-angle graphene

Disha Hou,[1] Yuhai Liu,[2] Toshihiro Sato,[3] Fakher F. Assaad,[3,4,*] Wenan Guo,[1,5,6,†] and Zhenjiu Wang[7,8,‡]

[1]*Department of Physics, Beijing Normal University, Beijing 100875, China*
[2]*School of Science, Beijing University of Posts and Telecommunications, Beijing 100876, China*
[3]*Institut für Theoretische Physik und Astrophysik, Universität Würzburg, 97074 Würzburg, Germany*
[4]*Würzburg-Dresden Cluster of Excellence ct.qmat, Am Hubland, 97074 Würzburg, Germany*
[5]*Key Laboratory of Multiscale Spin Physics (Ministry of Education), Beijing Normal University, Beijing 100875, China*
[6]*Beijing Computational Science Research Center, 10 East Xibeiwang Road, Beijing 100193, China*
[7]*Arnold Sommerfeld Center for Theoretical Physics, University of Munich, Theresienstrasse 37, 80333 Munich, Germany*
[8]*Max-Planck-Institut für Physik komplexer Systeme, 01187 Dresden, Germany*

(Received 2 May 2023; revised 15 August 2023; accepted 12 April 2024; published 7 May 2024)

We carry out large-scale quantum Monte Carlo simulations of a candidate field theory for the onset of superconductivity in magic-angle twisted bilayer graphene. The correlated insulating state at charge neutrality spontaneously breaks U(1) Moiré valley symmetry. Owing to the topological nature of the bands, skyrmion defects of the order parameter carry charge $2e$ and condense upon doping. In our calculations we encode the U(1) symmetry by an internal degree of freedom such that it is not broken upon lattice regularization. Furthermore, the skyrmion carries the same charge. The nature of the doping-induced phase transitions depends on the strength of the easy-plane anisotropy that reduces the SU(2) valley symmetry to $\mathrm{U}(1) \times \mathbb{Z}_2$. For large anisotropy, we observe two distinct transitions separated by phase coexistence. While the insulator to superconducting transition is of mean-field character, the U(1) transition is consistent with three-dimensional XY criticality. Hence, the coupling between the gapless charge excitations of the superconducting phase and the XY order parameter is irrelevant. At small anisotropy, we observe a first-order transition characterized by phase separation.

DOI: 10.1103/PhysRevB.109.195122

I. INTRODUCTION

Magic-angle twisted bilayer graphene (MATBG) provides a new platform to study correlation-induced phenomena. Aside from correlated insulating states at commensurate fillings, it is of great present interest to understand the physics when the electron filling factor is close to charge neutrality [1]. In particular, extensive attention has been paid in understanding how the correlated insulator gives way to a superconducting state via doping. Aside from transport properties [2,3], there is a lack of experimental tools [4] to study these two phases. A theoretical hypothesis from Refs. [5,6] attempts to explain the two states within a unifying framework. In this framework the SU(2) valley symmetry is weakly broken down to $\mathrm{U}(1) \times \mathbb{Z}_2$. The so-called Kramer intervalley coherent insulator (K-IVC) [7] spontaneously breaks the U(1) charge conservation within each Moiré valley; skyrmion defects of the order parameter carry electron charge $2e$, which, upon doping condense and trigger superconductivity [5,6,8]. The success of this continuum limit picture relies crucially on the conservation of valley quantum numbers corresponding to the *chiral* symmetry.

In constructing an effective lattice Hamiltonian for the above, a major difficulty arises since the valley (or chiral) symmetry will invariably be broken by the regularization. On the lattice, Dirac cones cannot be rotated independently. Furthermore, within the theory proposed in Ref. [5] the spin does not play a key role in the pairing mechanism, and in fact, spinless versions of the theory were put forward in Ref. [8]. In this article we propose to *swap* chiral and spin symmetries. We use the spin degree of freedom to encode the (Moiré) valley degrees of freedom and the two Moiré valley bands are reformulated in our case as physical spin (up and down). It follows naturally that, see Appendix A, the $\mathrm{U}(1) \times \mathbb{Z}_2$ symmetry-broken states (K-IVC and Valley Hall [7]) map onto a dynamically generated quantum spin Hall (QSH) insulator with easy-plane anisotropy. From previous works, see Refs. [10–12], it is known that skyrmion excitations of the QSH order parameter carry charge $2e$. In fact, in the absence of easy-plane anisotropy, it was argued in Ref. [12] that the proliferation of skyrmions simultaneously destroys the QSH order and generates superconductivity (SC) as the system is doped. Hence, the low-energy physics of MATBG can be realized by including easy-plane anisotropy, such that merons, as opposed to skyrmions, become the low-energy charged textures.

*assaad@physik.uni-wuerzburg.de
†waguo@bnu.edu.cn
‡Zhenjiu.Wang@physik.uni-muenchen.de

Although there is no essential difference between (pairs of) merons and skyrmions in terms of the defining topology and their associated electron charges, the symmetry difference between U(1) $\times \mathbb{Z}_2$ and SU(2) can lead to dramatic effects. Depending upon the easy axis anisotropy, meron (pairs) may have a large excitation gap and eventually, result in a doping-induced phase transition of mean-field character. This article aims at revealing the Cooper-pair condensation when doping a U(1) broken symmetry K-IVC insulator and at understanding the interplay between the two order parameter fluctuations.

II. MODEL AND METHOD

We consider a model of Dirac fermions in $2+1$ dimensions on the honeycomb lattice with Hamiltonian $\hat{H} = \hat{H}_t + \hat{H}_\lambda$. Here,

$$\hat{H}_t = -t \sum_{\langle i,j \rangle} (\hat{\boldsymbol{c}}_i^\dagger \hat{\boldsymbol{c}}_j + \text{H.c.}). \tag{1}$$

The spinor $\hat{\boldsymbol{c}}_i^\dagger = (\hat{c}_{i,+}^\dagger, \hat{c}_{i,-}^\dagger)$ where $\hat{c}_{i,\tau}^\dagger$ creates an electron at lattice site $\boldsymbol{i}$ with z-component of the internal degree of freedom $\boldsymbol{\tau}$, and the sum runs over the nearest neighbors of the honeycomb lattice

$$\hat{H}_\lambda = -\lambda \sum_{\hexagon} \sum_{\alpha=x,y,z} \Delta^\alpha \left(\sum_{\langle\langle ij \rangle\rangle \in \hexagon} \hat{J}_{i,j}^\alpha \right)^2, \tag{2}$$

where $\hat{\boldsymbol{J}}_{i,j} \equiv i\nu_{ij} \hat{\boldsymbol{c}}_i^\dagger \boldsymbol{\tau} \hat{\boldsymbol{c}}_j + \text{H.c.}$, with $\boldsymbol{\tau} = (\tau^x, \tau^y, \tau^z)$ the Pauli spin matrices, see the inset of Fig. 1. This term is a plaquette interaction involving next-nearest-neighbor pairs of sites and phase factors $\nu_{ij} = \pm 1$ identical to the Kane-Mele model [13], see also Ref. [11]. Finally, the easy-plane anisotropy is imposed by choosing $\boldsymbol{\Delta} = (1, 1, \Delta)$.

The SU(2) invariant version ($\Delta = 1$) of this Hamiltonian has been well studied in Refs. [11,12]. Associating τ to the spin degree of freedom, a dynamically generated QSH insulator that spontaneously breaks SU(2) τ-rotational symmetry is found at intermediate interacting strength (λ) and at half-filling. An SSC can be realized by increasing λ or doping. For $\Delta < 1$, we realized a U(1) symmetry-broken QSH state by reducing the full τ-rotational symmetry of the Hamiltonian [9].

The Hamiltonian we considered here captures the key ingredients of MATBG around charge neutrality. In MATBG, the Chern number of the flat bands is associated with the (Moiré) valley quantum number [7]. As documented in Appendix A the spin degrees of freedom in our toy model play the role of the (Moiré) valley in their case. Therefore, the Kramers intervalley coherent phase, which breaks spontaneously the U(1) valley symmetry is not different than our QSH insulator from a symmetry point of view. The following consequence from this symmetry argument is that in both cases, electron pairing arises from Kramers doublet based on pairs of meron configurations in the U(1) broken insulator. Upon doping, these preformed pairs condensate and superconductivity is formed. Crucially, although charge conservation within each valley (e.g., chiral symmetry) is an exact symmetry in the continuum limit, it is generically not possible realize it in a lattice Hamiltonian. A simple way of performing this regularization is to substitute the valley degrees of freedom with spin ones [14].

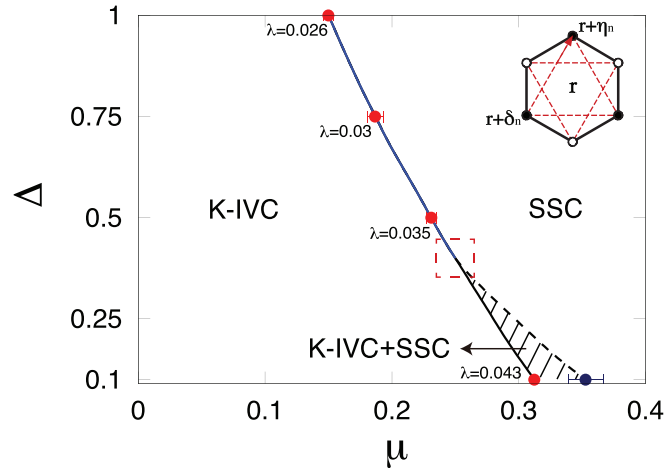

FIG. 1. Schematic phase diagram in the anisotropy Δ and chemical potential μ plane. For each value of Δ we consider a value of λ that maximizes the K-IVC order at charge neutrality ($\mu = 0$), as determined in [9]. Since the K-IVC is an insulting phase, a critical chemical potential is needed to obtain a metallic state. This critical potential is given by the black and blue lines. Blue line indicates first-order phase transition, while black lines, solid, and dashed, indicate continuous ones. Hence, for values of Δ and μ confined to the blue line the compressibility diverges and the phase separation between the K-IVC and SSC states is expected. The black dashed line denotes K-IVC + SSC to the SSC transition. Red bullets denote the superconducting transition points while the blue dot corresponds to the K-IVC + SSC to SSC transition point. The box with dashed line indicates the uncertainty in identifying the position of critical end point, which depends on the specific choice of λ at each value of Δ. The inset illustrates the spin-orbit interactions inside a plaquette.

Here we focus on the case where $\Delta \in [0, 1)$ such that the SU(2) spin rotational symmetry is reduced to U(1) $\times \mathbb{Z}_2$. We investigate three values of the anisotropy and only consider values of λ deep inside the charge-neutral K-IVC state [9]: $\lambda = 0.043$ for $\Delta = 0.1$, $\lambda = 0.035$ for $\Delta = 0.5$, and $\lambda = 0.03$ for $\Delta = 0.75$. This Δ-dependent value of λ is chosen so as to guarantee that at μ the charge gap is maximal. Our unit of energy is set by $t = 1$.

We use the algorithms for lattice fermions (ALF) implementation [15] of the auxiliary-field quantum Monte Carlo (QMC) method [16–18]. Because $\lambda > 0$ and $\Delta > 0$, a real Hubbard-Stratonovich decomposition for the perfect square term does not break the time-reversal symmetry. Since charge is conserved, the eigenvalues of the fermion determinant come in complex conjugate pairs such that no sign problem occurs [19]. We simulate periodic systems with size of $L \times L$. The imaginary time interval is $\Delta\tau = 0.2$ and a symmetric Trotter decomposition is chosen to ensure the hermiticity of the Trotterized imaginary time evolution [11]. Additionally, we apply a checkerboard decomposition to the exponential of hopping matrix $\hat{H}_t$. Following our previous work [12], we use a projective QMC algorithm (PQMC) [18,20,21]. For the trial wave function, we take the ground state of the hopping Hamiltonian in Eq. (1) with spin-dependent twisted boundary

conditions. This Slater determinant is then uniquely defined and also time-reversal symmetric.

III. QMC RESULTS

To capture the K-IVC order, we define the local operators $\hat{\boldsymbol{O}}_{\boldsymbol{r},n} \equiv \hat{\boldsymbol{J}}_{\boldsymbol{r}+\boldsymbol{\delta}_n,\boldsymbol{r}+\boldsymbol{\eta}_n}$. Here, $\boldsymbol{r}$ denotes a unit cell and $n = 1, 2, \ldots, 6$ are the six next-nearest-neighbor bonds of the corresponding hexagon with legs $\boldsymbol{r}+\boldsymbol{\delta}_n$ and $\boldsymbol{r}+\boldsymbol{\eta}_n$. The K-IVC order with broken U(1) rotational symmetry is detected by computing

$$S^{\text{K-IVC}}_{m,n}(\boldsymbol{q}) \equiv \frac{1}{L^2}\sum_{\boldsymbol{r},\boldsymbol{r}'} e^{i\boldsymbol{q}\cdot(\boldsymbol{r}-\boldsymbol{r}')}\langle \hat{O}^X_{\boldsymbol{r},m}\hat{O}^X_{\boldsymbol{r}',n} + \hat{O}^Y_{\boldsymbol{r},m}\hat{O}^Y_{\boldsymbol{r}',n}\rangle, \quad (3)$$

with $m, n = 1, 2, \ldots, 6$.

As for SSC we consider

$$S^{\text{SSC}}_{a,b}(\boldsymbol{q}) \equiv \frac{1}{L^2}\sum_{\boldsymbol{r},\boldsymbol{r}'} e^{i\boldsymbol{q}\cdot(\boldsymbol{r}-\boldsymbol{r}')}\left[\left\langle \hat{\eta}^+_{\boldsymbol{r},\tilde{\boldsymbol{\delta}}_a}\hat{\eta}^-_{\boldsymbol{r}',\tilde{\boldsymbol{\delta}}_b}\right\rangle + \left\langle \hat{\eta}^-_{\boldsymbol{r},\tilde{\boldsymbol{\delta}}_a}\hat{\eta}^+_{\boldsymbol{r}',\tilde{\boldsymbol{\delta}}_b}\right\rangle\right], \quad (4)$$

where $a, b = 1, 2$, denotes the A (B) sublattices, and $\hat{\eta}^+_{\boldsymbol{r},\tilde{\boldsymbol{\delta}}_a} = \hat{c}^\dagger_{\boldsymbol{r}+\tilde{\boldsymbol{\delta}}_a,+}\hat{c}^\dagger_{\boldsymbol{r}+\tilde{\boldsymbol{\delta}}_a,-}$.

The corresponding renormalization-group invariant correlation ratio reads

$$R^O \equiv 1 - \frac{S^O(\boldsymbol{q}_0+\delta\boldsymbol{q})}{S^O(\boldsymbol{q}_0)}, \quad (5)$$

where S^O is the largest eigenvalue of the corresponding correlation matrix (O = K-IVC, SSC). $\boldsymbol{q}_0$ is the ordering wave vector and $\boldsymbol{q}_0+\delta\boldsymbol{q}$ is the neighboring wave vector ($|\delta\boldsymbol{q}| = \frac{4\pi}{\sqrt{3}L}$).

We define the doping factor δ by the density of doped holes relative to charge neutrality $\delta \equiv \frac{2L^2-N_e}{2L^2}$. Here, N_e counts the number of electrons. Due to large autocorrelation times related to particle fluctuations, it is convenient to adopt a canonical ensemble. Within this ensemble, the chemical potential is evaluated from the ground-state energy difference between nearby charge sectors

$$\mu \equiv \frac{\Delta_{\eta^-}(N_e)}{2}. \quad (6)$$

Here, $\Delta_{\eta^-}(N_e)$ is the pairing (η^-) gap extrapolated from the time-displaced correlation function.

Our results are summarized in the ground-state phase diagram in the Δ versus μ plane, as shown in Fig. 1. For each value of Δ we consider a coupling λ that places us well within the correlated insulating phase at charge neutrality [9]. Below we will document that at small anisotropy we observe a first-order transition characterized by phase separation between the K-IVC and SSC. At large anisotropy, phase coexistence sets in.

Figures 2 and 3 show the correlation ratios for the SSC and K-IVC instabilities at $\Delta = 0.1$ and $\Delta = 0.5$. As is apparent, the K-IVC order survives finite doping, with the critical doping, $\delta_c^{\text{K-IVC}}$, being given by the crossing point of the curves. On the other hand, superconductivity sets in at any finite doping for both considered values of the anisotropy, Δ. Since we are working in a canonical ensemble, we have to check for the stability against phase separation as signaled by an infinite

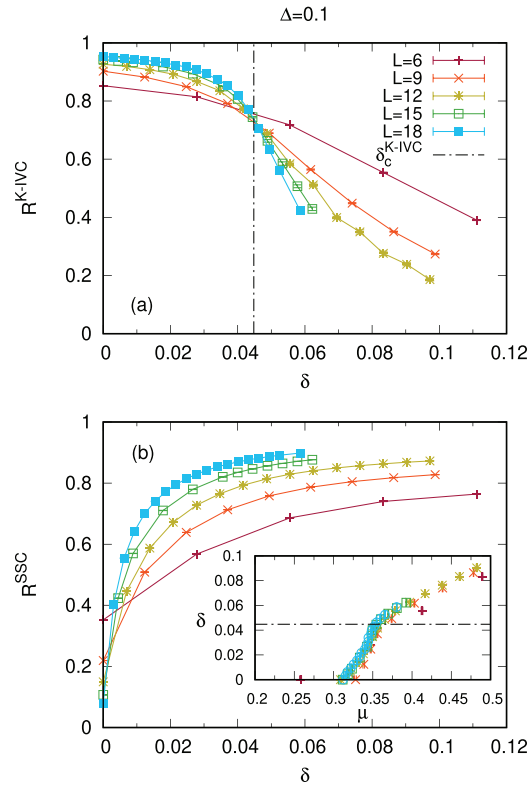

FIG. 2. Equal-time correlation ratio for (a) $R^{\text{K-IVC}}$ and (b) R^{SSC} as a function of doping factor δ for $\Delta = 0.1$. The vertical dashed line in (a) is a guide to the eye, fitted from the crossing point of K-IVC order parameter between $L = 15$ and 18. The inset of (b) shows the doping factor δ as a function of chemical potential μ in this case. The horizontal dashed line is the same as the vertical one in (a).

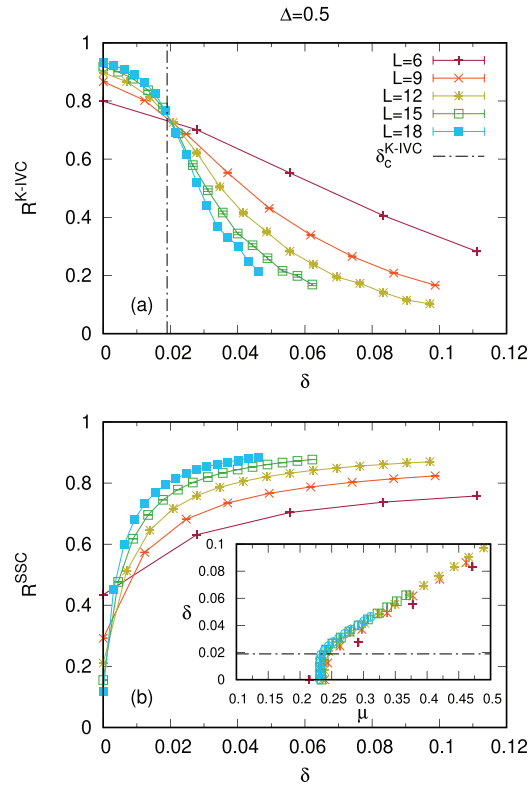

FIG. 3. Same as Fig. 2, for $\Delta = 0.5$.

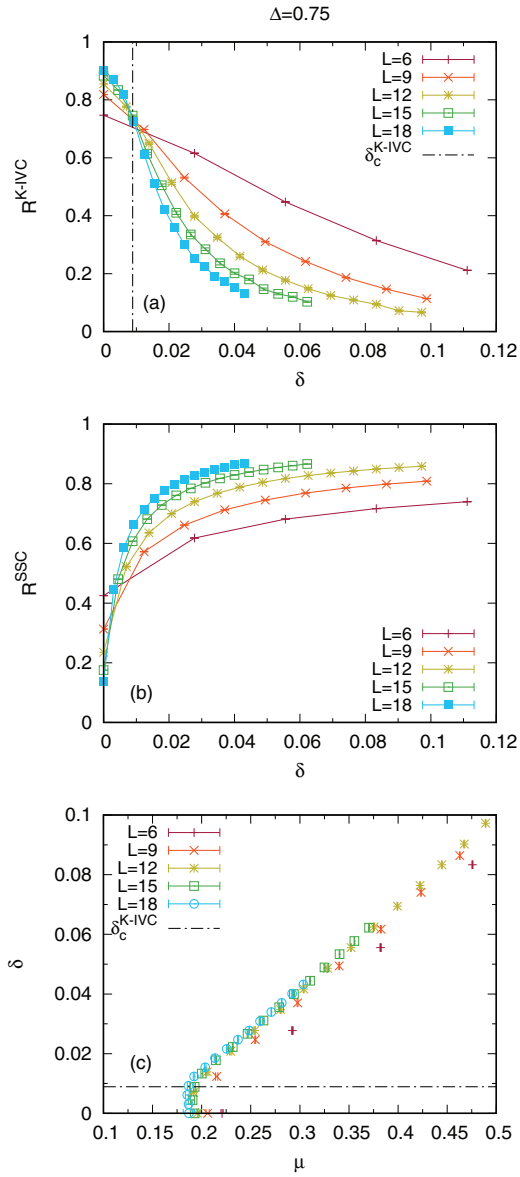

FIG. 4. Same as Fig. 2, for $\Delta = 0.75$.

compressibility $\frac{\partial\delta}{\partial\mu}$. The inset in Fig. 3(b) plots this quantity at $\Delta = 0.5$. As is apparent, in the range $0 < \delta < \delta_c^{\text{K-IVC}}$ the data are consistent with a diverging compressibility. Hence, in this doping range and in the thermodynamic limit, we expect to observe puddles of K-IVC insulating phases with a total density set by $1 - \frac{\delta}{\delta_c^{\text{K-IVC}}}$ and regions of SSC with a total density set by $\frac{\delta}{\delta_c^{\text{K-IVC}}}$ [22].

The data for $\Delta = 0.75$ are presented in Figs. 4(a)–4(c). The data bear strong similarities to the case of $\Delta = 0.5$. In particular, we observe a first-order phase transition between the K-IVC and SSC. However, in comparison to the case $\Delta = 0.5$ we see that the doping range where phase separation occurs $0 < \delta < \delta_c^{\text{K-IVC}}$ is smaller.

The fact that skyrmions in S^2 space carry charge $2e$ can be imaged locally: electron densities are associated with the curvature of the local spin-orbit fluctuations. Correspondingly, spin current textures will also be observed when the electron

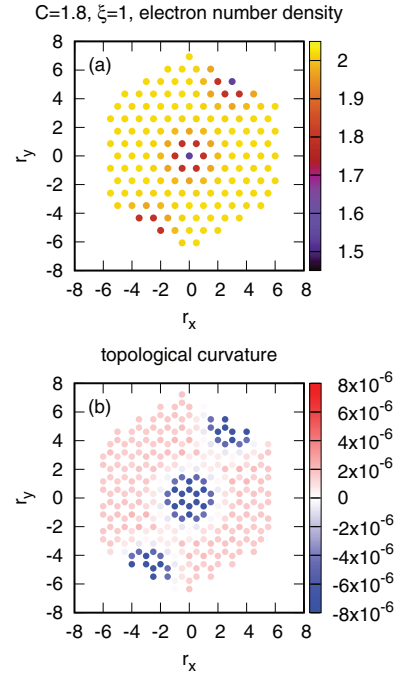

FIG. 5. (a) Electron particle number distribution in each unit cell and (b) the curvature in S^2 space of spin current in the presence of a finite pinning potential based on Eq. (7). The simulation is performed on a 12×12 lattice with $\delta = 2/288$, $\Delta = 0.75$, and $\lambda = 0.03$.

(hole) distribution is not uniform. The one-to-one relation between these two quantities can be demonstrated by trapping a pair of holes at two separate regions of the honeycomb lattice by adding a site-dependent pinning potential:

$$H_{pin} = C \sum_{\boldsymbol{r}} \sum_{\tilde{\boldsymbol{\delta}}} \exp(-|\boldsymbol{r} - \boldsymbol{r}_{c_1} + \tilde{\boldsymbol{\delta}}|/\xi) \hat{c}^{\dagger}_{\boldsymbol{r}+\tilde{\boldsymbol{\delta}}} \hat{c}_{\boldsymbol{r}+\tilde{\boldsymbol{\delta}}} + C \sum_{\boldsymbol{r}} \sum_{\tilde{\boldsymbol{\delta}}} \exp(-|\boldsymbol{r} - \boldsymbol{r}_{c_2} + \tilde{\boldsymbol{\delta}}|/\xi) \hat{c}^{\dagger}_{\boldsymbol{r}+\tilde{\boldsymbol{\delta}}} \hat{c}_{\boldsymbol{r}+\tilde{\boldsymbol{\delta}}}, \quad (7)$$

such that the electron density relative to half-filling is reduced around the center of two potential wells $\boldsymbol{r}_{c1}$ and $\boldsymbol{r}_{c2}$, as shown by Fig. 5(a).

Correspondingly, the curvature of the spin-orbit order parameter is given by

$$C_{\boldsymbol{r}} = \frac{1}{4\pi} \hat{\boldsymbol{J}}_{\boldsymbol{r}} \cdot (\partial_x \hat{\boldsymbol{J}}_{\boldsymbol{r}} \times \partial_y \hat{\boldsymbol{J}}_{\boldsymbol{r}}) = \frac{1}{4\pi \mathcal{A}} \det \begin{pmatrix} \hat{J}^X_{\boldsymbol{r},m=1} & \hat{J}^X_{\boldsymbol{r}+\boldsymbol{a}_1,m=2} & \hat{J}^X_{\boldsymbol{r}+\boldsymbol{a}_2,m=3} \\ \hat{J}^Y_{\boldsymbol{r},m=1} & \hat{J}^Y_{\boldsymbol{r}+\boldsymbol{a}_1,m=2} & \hat{J}^Y_{\boldsymbol{r}+\boldsymbol{a}_2,m=3} \\ \hat{J}^Z_{\boldsymbol{r},m=1} & \hat{J}^Z_{\boldsymbol{r}+\boldsymbol{a}_1,m=2} & \hat{J}^Z_{\boldsymbol{r}+\boldsymbol{a}_2,m=3} \end{pmatrix}, \quad (8)$$

where $\boldsymbol{r}$ denotes the position of the unit cell and m labels the six next-nearest-neighbor bonds. We use $m = 1, 2, 3$, respectively, on hexagons at site $\boldsymbol{r}$, $\boldsymbol{r} + \boldsymbol{a}_1$, and $\boldsymbol{r} + \boldsymbol{a}_2$, as shown in Fig. 6. Here $\mathcal{A}$ is the area of a hexagon. This way of defining curvature is to avoid explicit density operators via the commutator of spin current operators. From Fig. 5(b), it is clear that the curvature distribution in real space follows exactly the spatial pattern of the electron density.

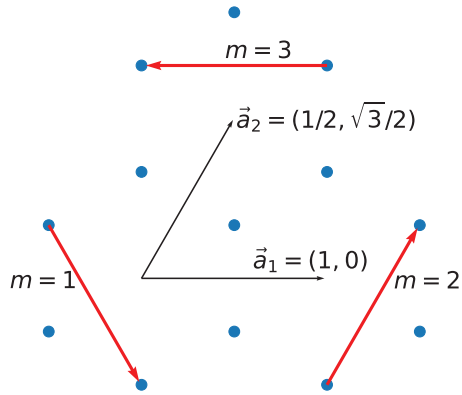

FIG. 6. Definition of the three next-nearest-neighbor bonds $m = 1, 2, 3$ used for defining the curvature operator in Eq. (8).

On the other hand, at strong anisotropy, $\Delta = 0.1$, the inset of Fig. 2(b) shows no sign of diverging compressibility, thus indicating phase coexistence. However, we observe two nonanalytical points at $\mu_{c1} \approx 0.31$ and $\mu_{c2} \approx 0.35$ that corresponds to the insulator to superconductor transition at $\delta = 0^+$ and to the K-IVC transition at $\delta = \delta_c^{\text{K-IVC}}$. Both transitions show no features of first-order transitions, as can be directly seen from the continuous behavior of $\delta - \mu$ dependence in Fig. 2(b). We note that, at the superconducting transition at μ_{c1}, the hyperscaling law

$$\delta - \delta_c \propto |\mu - \mu_c|^{\nu d}, \quad \nu z = 1, \tag{9}$$

holds. This is due to the fact that the generator of the SSC order parameter couples to the chemical potential μ, corresponding to the tuning parameter of this quantum phase transition [23].

The linear δ-μ dependence at $\mu_{c1} \approx 0.31$ in Fig. 2(b) suggests that $z = 2$ at the superconducting phase transition. Assuming that the background of K-IVC ordering does not couple to any critical fluctuations at the superconducting critical point, a mean-field phase transition with $z = 2$, $\nu = 0.5$ at μ_{c1} is expected. This transition is in the very same universality class as that of the Mott-insulator-superfluid transition in the doped Bose-Hubbard system [23].

To understand the nature of the K-IVC transition in the background of superconducting order, we fit our data to the following form:

$$\begin{aligned} R^{\text{K-IVC}} &= f_1\big[(\delta - \delta_c^{\text{K-IVC}})L^{1/\nu}\big], \\ m^{\text{K-IVC}} L^{(z+\eta)/2} &= f_2\big[(\delta - \delta_c^{\text{K-IVC}})L^{1/\nu}\big], \end{aligned} \tag{10}$$

where $m^{\text{K-IVC}} \equiv \sqrt{\sum_n S_{n,n}^{\text{K-IVC}}(\boldsymbol{q}_0)/L^2}$ is the K-IVC order parameter. Our results, Fig. 7, suggest that the transition is consistent with Lorentz invariance, $z = 1$, and that it falls into the three-dimensional (3D) XY universality class. In particular, we consider $\nu \approx 0.67169$ and $\eta \approx 0.03810$ from previous Monte Carlo simulations of the 3D XY model [24] as well as $\delta_c^{\text{K-IVC}} = 0.0448$ for our data collapse. As shown in Fig. 7, both quantities show nice collapse for system sizes from $L = 6$ to $L = 18$.

We also perform a collective polynomial fit using $L = 15$ and 18 based on Eq. (10). The results are listed in Table I.

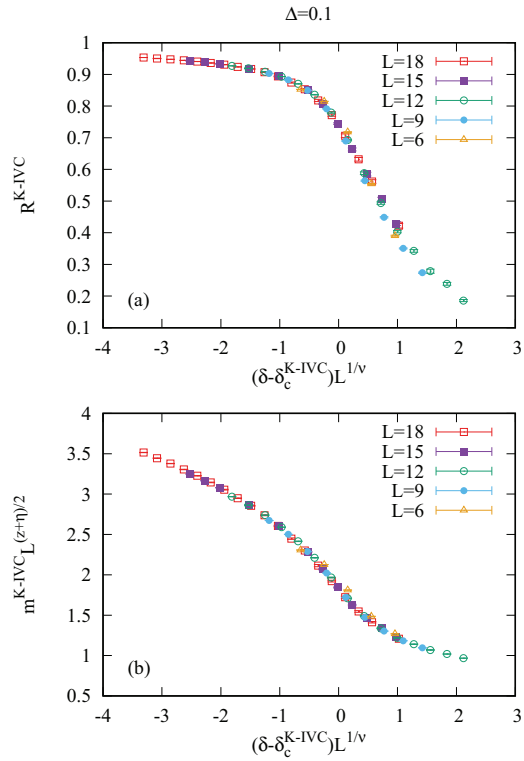

FIG. 7. Data collapse at $\Delta = 0.1$ with $\delta_c^{\text{K-IVC}} = 0.0448$ and 3D XY exponent whose $\nu = 0.67169(7)$, $\eta = 0.03810(8)$ for (a) the correlation ratio and (b) the K-IVC order parameter.

Even when a wide fitting range is taken into consideration, the value of ν that we obtain is consistent with 3D XY universality class.

An interesting question to ask is why symmetry-allowed coupling terms between the K-IVC order parameter and the critical charge fluctuations of the superconductor play no role at the 3D XY phase transition. In Appendix B we provide a power counting argument to show that the Goldstone modes of the SSC order parameter are irrelevant at the 3D XY fixed point.

IV. DISCUSSION AND SUMMARY

We consider an effective lattice model that captures the physics of a candidate theory of MATBG [5], which unifies the K-IVC insulator and superconducting phases: skyrmions defect of the K-IVC order parameter carry charge $2e$ and condense upon doping. The key insight to obtaining lattice regularization of this physics is to encode the valley symmetry with the spin degree of freedom. In Appendix C we show that the single-particle gap does not vanish. This allows us to integrate out the electronic degrees of freedom

TABLE I. ν fitting of K-IVC vanishing transition.

Order	L	$(\delta - \delta_c^{\text{K-IVC}})L^{1/\nu}$	ν	χ_r^2/DOF	Observable
13	[15:18]	[−2.8:1.05]	0.67(1)	1.19/16	$R^{\text{K-IVC}}$
7	[15:18]	[−2.58:1.05]	0.67(1)	1.39/15	$m^{\text{K-IVC}}$

and precisely obtain the low-energy topological field theory presented in Ref. [5]. Large-scale QMC simulations reveal two different types of transitions depending upon the strength of the easy-plane anisotropy. At large anisotropy we observe phase coexistence. As a function of doping the insulating state gives way to a superconducting phase, with the universality class being identical to that of the Bose-Hubbard model [23]. At larger doping, we observe the vanishing of the U(1) order in the background of the superconducting phase. Our results show that this phase transition belongs to the 3D XY universality class, such that coupling to gapless charge fluctuations are irrelevant at this critical point.

For the small anisotropic case, we observe phase separation. In conjunction with our previous results for the SU(2) case [12], we observe that the doping range in which phase separation occurs decreases as one approaches the SU(2) symmetric point, $\Delta \to 1$. This challenges the conclusion of Ref. [12] where a seemingly continuous transition with large dynamical exponent was observed. Alternatively, if symmetry plays a crucial role, an interesting possibility is that the large z continuous transition only exists in the SU(2) symmetric case. Our parameters are such that the single-particle gap at charge neutrality is independent of the anisotropy and the pairing gap decreases as the anisotropy grows, see Appendix D. We interpret this in terms of meron pairs that become energetically more expensive due to a smaller core size at strong anisotropy. It is hence tempting to interpret the phase diagram of Fig. 1 as dominated by topology in the vicinity of the SU(2) symmetric point and from the point of view of a Ginzburg-Landau theory at strong anisotropy. This statement is substantiated by calculations at small anisotropy, which show the locking of the charge density and curvature of the K-IVC order parameter.

The s-wave superconducting state is adiabtically connected to a conventional BCS superconductor. Thus there is no sharp distinction between skyrmion and BCS superconductivity. However, the smoking gun evidence of the skyrmion-induced pairing is shown in Ref. [12] for the SU(2) case at $\Delta = 1$ and in Sec. III of this work: the visualization of skyrmion configurations when trapping a pair of holes in charge potential wells.

Let us now return to MATBG, where the easy-plane anisotropy is expected to be small [7]. The numerical study in Ref. [8] suggested that the mechanism of skyrmion superconductivity is stable to the Coulomb repulsion, such that our model can very well capture the low-energy physics of MATBG. In this case, our results suggest that the doping-induced transition is first order and entails phase separation.

ACKNOWLEDGMENTS

Z.W. thanks Benoit Doucot and Peng Rao for enlightening conversations. The authors gratefully acknowledge the Gauss Centre for Supercomputing e.V. for funding this project by providing computing time on the GCS Supercomputer SUPERMUC-NG at Leibniz Supercomputing Centre. F.F.A. acknowledges the DFG for funding via the Würzburg-Dresden Cluster of Excellence on Complexity and Topology in Quantum Matter ct.qmat (EXC 2147, Project ID 390858490) as well as the SFB1170 on Topological and Correlated Electronics at Surfaces and Interfaces. D.H. and W.G. were supported by the National Natural Science Foundation of China under Grants No. 12175015 and No. 11734002. T.S. acknowledges funding from the Deutsche Forschungsgemeinschaft under Grant No. SA 3986/1-1. Y.L. was supported by the National Natural Science Foundation of China under Grant No. 12305039 and the Fundamental Research Funds for the Central Universities from the Beijing University of Posts and Telecommunications under Grant No. 2023RC42. Z.W. was supported by the FP7/ERC Consolidator Grant QSIMCORR, No. 771891.

APPENDIX A: RELATION TO MAGIC-ANGLE TWISTED BILAYER GRAPHENE

Our model is closely analogous to those described in Refs. [5,7] that aim at accounting for superconductivity resulting from the condensation of skyrmions in magic-angle twisted bilayer graphene (MATBG). The starting point is the Bistritzer-MacDonald continuum model [25] in the chiral limit, in which interlayer hopping between the same sublattice is set to zero. In this case, the low-lying bands are flat and can be labeled by sublattice polarization, which is complete in this limit, as well as a valley and spin index. In this basis, the bands carry nontrivial topology characterized by a Chern number. Let $\hat{c}^\dagger_{\tau,\sigma,s}(\boldsymbol{k})$ create an electron with momentum $\boldsymbol{k} + \boldsymbol{K}_\tau$, in valley τ, sublattice polarization σ, and physical spin s. The Chern number of the bands is given by $\sigma_z\tau_z$. In this chiral limit, the form factor of the density fluctuations depends solely on $\sigma_z\tau_z$, such that the complete model possesses a U(4) $\times$ U(4) symmetry that rotates the bands in a given Chern sector. This model captures the dominant energy scales. Perturbations beyond the chiral limit break this symmetry. In fact, the phases and phase transitions discussed in Refs. [5,7] are captured by the effective model

$$\begin{aligned}\hat{H} = &\sum_{\boldsymbol{k}} \hat{c}^\dagger(\boldsymbol{k})(k_x\sigma^x + k_y\sigma^y\tau^z)\hat{c}\ (\boldsymbol{k}) \\ &-\lambda\int_V d^2\boldsymbol{x}\hat{P}([\hat{c}^\dagger(\boldsymbol{x})\tau^x\sigma^y\hat{c}\ (\boldsymbol{x})]^2 \\ &+[\hat{c}^\dagger(\boldsymbol{x})\tau^y\sigma^y\hat{c}\ (\boldsymbol{x})]^2 + \Delta[\hat{c}^\dagger(\boldsymbol{x})\sigma^z\hat{c}\ (\boldsymbol{x})]^2)\hat{P}.\end{aligned} \tag{A1}$$

Here, $\hat{P}$ reflects the projection onto the low-energy Hilbert space. To be more precise, let $|\boldsymbol{k},\tau,\sigma,s\rangle = \hat{c}^\dagger_{\tau,\sigma,s}(\boldsymbol{k})|0\rangle$ such that the resolution of unity in the single-particle Hilbert space reads $\hat{1} = \sum_{\boldsymbol{k},\tau,\sigma,s}|\boldsymbol{k},\tau,\sigma,s\rangle\langle\boldsymbol{k},\tau,\sigma,s| + \hat{P}_H$, where $\hat{P}_H$ denotes the projection on the high-energy states. Then, $\hat{c}^\dagger_{\tau,\sigma,s}(\boldsymbol{x}) = \sum_{\boldsymbol{k},\tau,\sigma,s}\langle\boldsymbol{k},\tau,\sigma,s|\boldsymbol{x},\tau,\sigma,s\rangle\hat{c}^\dagger_{\tau,\sigma,s}(\boldsymbol{k})$. As mentioned above, the single-particle wave functions of flat bands $|\boldsymbol{k},\tau,\sigma,s\rangle$ have a characteristic Chern number of $\tau_z\sigma_z$. Crucially, $\hat{c}^\dagger_{\tau,\sigma,s}(\boldsymbol{x})$ does not satisfy the fermion canonical commutation rules since the transformation is not unitary. $\boldsymbol{M}^{\mathrm{VH}} = (\tau^x\sigma^y, \tau^y\sigma^y, \sigma^z)$ correspond to mutually anticommuting mass terms that account for the so-called Kramers intervalley-coherent (K-IVC) and valley-Hall (VH) insulators.

At $\Delta = 1$ the model has an $\mathrm{SU}_V(2)$ *valley* symmetry with generators $\frac{i}{2}[M_i^{\mathrm{VH}}, M_j^{\mathrm{VH}}]$, corresponding to $(\tau^x\sigma^x, \tau^y\sigma^x, \tau^z)$, as well as an $\mathrm{SU}_S(2)$ spin symmetry and a $\mathrm{U}_C(1)$ charge symmetry. For $\Delta \neq 1$, the $\mathrm{SU}_V(2)$ symmetry is reduced to a $\mathrm{U}_V(1) \times \mathrm{Z}_2$ and for $\Delta < 1$ the K-IVC state is favored. Since

the bands have a nontrivial Chern index, skyrmion excitations of the three-component K-IVC and VH order parameters carry charge $2e$. We note that, since the $SU_V(2)$ is reduced to $U_V(1) \times Z_2$, the skyrmions have to be seen in terms of a pair of merons, each carrying charge e. Hence, all in all, the model has $U_V(1) \times Z_2 \times U_C(1) \times SU_s(2)$ symmetry. The doping-induced transition between the K-IVC and SSC put forward in Ref. [5] and based on the proliferation of skyrmions, does not involve the spin degrees of freedom. Spinless versions of the model have been put forward to capture the relevant physics [5,8].

The model of Eq. (A1) does not support lattice regularization since it will break the valley (or chiral) symmetry. Furthermore, the topology of the bands does not allow for a local Wannier basis. As a result, simulations of MATBG are carried out in the continuum [8,26,27]. Our model provides a possibility to avoid this by encoding the $SU_V(2)$ symmetry as $SU_S(2)$. A continuum limit of our model reads

$$\begin{aligned}\hat{H} = &\sum_{\boldsymbol{k}} \hat{c}^\dagger(\boldsymbol{k})(k_x\sigma^x + k_y\sigma^y\tau^z)\hat{c}\ (\boldsymbol{k}) \\ &- \lambda \int_V d^2\boldsymbol{x}([\hat{c}^\dagger(\boldsymbol{x})s^x\tau^z\sigma^z\hat{c}\ (\boldsymbol{x})]^2 \\ &+ [\hat{c}^\dagger(\boldsymbol{x})s^y\tau^z\sigma^z\hat{c}\ (\boldsymbol{x})]^2 + \Delta[\hat{c}^\dagger(\boldsymbol{x})s^z\tau^z\sigma^z\hat{c}\ (\boldsymbol{x})]^2),\end{aligned} \tag{A2}$$

where $\boldsymbol{M}^{\mathrm{QSH}} = (s^x, s^y, s^z)\tau^z\sigma^z$ correspond to the three QSH mass terms. The parallel now becomes apparent: the $\boldsymbol{M}_z^{\mathrm{QSH}}$ mass corresponds to the Valley Hall insulator, and the first two components to the K-IVC insulator. Topologically, both models are equivalent since the skyrmion of the three-component QSH order parameter carries charge $2e$. The symmetry of the Hamiltonian is given by $U_s(1) \times Z_2 \times U_C(1) \times SU_V(2)$. Here the $SU_V(2)$ symmetry is again spanned by the generators $(\tau^x\sigma^x, \tau^y\sigma^x, \tau^z)$.

APPENDIX B: SCALING ANALYSIS OF THE COUPLING BETWEEN TWO ORDER PARAMETERS

The aim of this Appendix is to show that at the 3D XY critical point coupling to charge fluctuations is irrelevant. To this end, we write down the φ^4 theory describing the K-IVC phase transition within the superconducting state

$$\mathcal{S} = \mathcal{S}_{\text{K-IVC}} + \mathcal{S}_{\text{SSC}} + \mathcal{S}_{\text{coupling}}, \tag{B1}$$

where $\mathcal{S}_{\text{K-IVC}}$ is the bare action for K-IVC field and $\mathcal{S}_{\text{SSC}}$ is the one for SSC order. Here we denote the two U(1) order parameters for K-IVC and SSC as $\boldsymbol{n}$ and ϕ, respectively. In the SSC phase, we can decompose the field as $\phi(\boldsymbol{x}) = |\phi(\boldsymbol{x})|\exp(i\theta(\boldsymbol{x}))$ with $|\phi(\boldsymbol{x})| = \phi_0 + \phi_\parallel(\boldsymbol{x})$. $\theta(\boldsymbol{x})$ represents the Goldstone mode of ϕ.

$\mathcal{S}_{\text{coupling}}$ describes the charge- or spin-neutral coupling terms between two fields. The leading term reads

$$g\int d^D r|\boldsymbol{n}|^2\partial_\mu\theta(\boldsymbol{x})\partial_\mu\theta(\boldsymbol{x}), \tag{B2}$$

where $D = d + 1$ and $d = 2$. Note that terms like $\int d^D r|\boldsymbol{n}|^2|\phi|^2$ will not be present at this critical point since ϕ has a finite mass along the longitudinal direction in the SSC phase.

Let Δ_n be the scaling dimension of the field $\boldsymbol{n}$ and Δ_θ be the scaling dimension of the Goldstone boson θ. According to standard scaling theory, the scaling dimension of λ should be $\Delta_\lambda = D - 2\Delta_n - 2(\Delta_\theta + 1)$.

Assume that in our system, the Wilson-Fisher fixed point of the field $\boldsymbol{n}$ belongs to the $2+1D$ universality class ($\Delta_n = \frac{D-2+\eta}{2} = 0.51905$, with $\eta = 0.03810$). On the other hand, the Goldstone mode θ of a superconducting state in $2+1D$ is associated with a power-law decay correlation function along the transverse direction

$$\langle e^{i\theta(\boldsymbol{r})}e^{i\theta(0)}\rangle \propto \int \frac{d^3k}{(2\pi)^3}\frac{i\boldsymbol{k}\cdot\boldsymbol{r}}{k^2} \propto \frac{1}{|\boldsymbol{r}|}. \tag{B3}$$

This is based on the saddle point expansion of φ^4 theory along the massless direction. Therefore, $\Delta_\theta = 0.5$, and as a consequence, $\Delta_\lambda = D - 2\Delta_n - 2\Delta_\theta - 2 < 0$. This implies that the coupling between two U(1) order parameters is irrelevant. This is consistent with our numerical evidence of the $2+1D$ O(2) universality class at the K-IVC critical point.

APPENDIX C: SINGLE-PARTICLE SPECTRUM

In this section, we show the single-particle spectrum at finite chemical potential. At zero temperature we can sharply distinguish between the particle addition and removal spectra:

$$\begin{aligned}A(\omega) &= A_+(\omega) + A_-(-\omega), \\ \langle c_{\boldsymbol{k},\sigma}(\tau)c^\dagger_{\boldsymbol{k},\sigma}(0)\rangle &= \int d\omega e^{-\tau\omega}A_+(\omega), \\ \langle c^\dagger_{\boldsymbol{k},\sigma}(\tau)c_{\boldsymbol{k},\sigma}(0)\rangle &= \int d\omega e^{-\tau\omega}A_-(\omega).\end{aligned} \tag{C1}$$

We obtain the spectral function by analytic continuation in particle and hole channels:

$$\begin{aligned}A(\boldsymbol{k},\omega) = &\frac{1}{Z}\sum_n[|\langle n|c_{\boldsymbol{k}}|0\rangle|^2\delta(E_n - E_0 - \omega)] \\ &+ \frac{1}{Z}\sum_m[|\langle m|c^\dagger_{\boldsymbol{k}}|0\rangle|^2\delta(E_m - E_0 + \omega)].\end{aligned} \tag{C2}$$

Here, $|0\rangle$ in Eq. (C2) is the ground state at finite doping and $\langle n|$ is an eigenstate of the Hamiltonian with energy E_n and an additional particle (hole) relative to the ground state. We use the stochastic Maxent [28] implementation of the ALF [15] library.

In Fig. 8, we plot the spectral functions for the $L = 18$ lattice and dopings $\delta = 0$, $\frac{6}{648}$, $\frac{14}{648}$, and $\frac{28}{648}$. As is apparent, we always observe a single-particle gap in the spectra and an approximate particle-hole symmetry around the Fermi level. At finite doping, this stems from the superconducting nature of the ground state and the energy cost of breaking a Cooper pair. Importantly, since fermion excitations are gapped, one can integrate them out to derive the purely bosonic field theory discussed in Ref. [5].

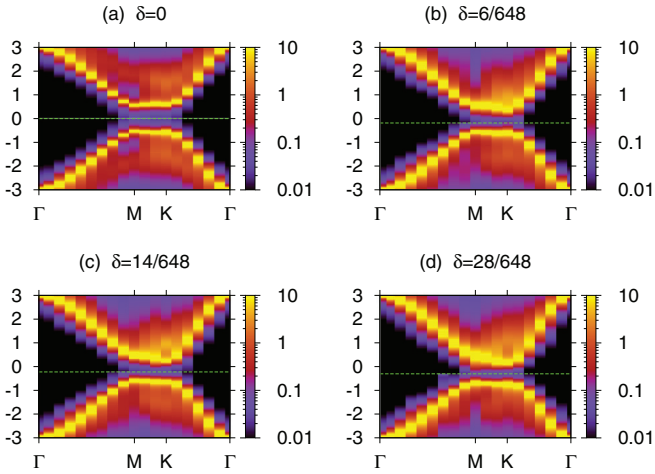

FIG. 8. Single-particle spectrum for several dopings at $\Delta = 0.75$. (a) $\delta = 0$ (inside K-IVC phase); (b) $\delta = \frac{6}{648}$ (around K-IVC-SSC transition); (c) $\delta = \frac{14}{648}$ (inside SSC phase); and (d) $\delta = \frac{28}{648}$ (inside SSC phase). The green dotted line corresponds to the chemical potential μ evaluated from Eq. (6) of the main text.

APPENDIX D: PREFORMED PAIRS

Here, we would like to clarify two points: (i) pairs of merons are the lowest-energy excitations and (ii) the gap of preformed pairs increases as a function of anisotropy.

We extrapolate the excitation energy of the pairing gap Δ_{SC} as obtained from the SSC imaginary-time correlations

$$\frac{1}{L^2}\sum_{\boldsymbol{r},\boldsymbol{r}'}\left[\langle\hat{\eta}^{+}_{\boldsymbol{r},\tilde{\boldsymbol{\delta}}_a}(\tau)\hat{\eta}^{-}_{\boldsymbol{r}',\tilde{\boldsymbol{\delta}}_b}(0)\rangle + \langle\hat{\eta}^{-}_{\boldsymbol{r},\tilde{\boldsymbol{\delta}}_a}(\tau)\hat{\eta}^{+}_{\boldsymbol{r}',\tilde{\boldsymbol{\delta}}_b}(0)\rangle\right] \propto e^{-\Delta_{SC}\tau}, \tag{D1}$$

as well as the fermionic single-particle gap from the Green's function

$$\sum_{\sigma}\langle c_{\boldsymbol{k},\sigma}(\tau)c^{\dagger}_{\boldsymbol{k},\sigma}(0)\rangle \propto e^{-\Delta_{sp}\tau}. \tag{D2}$$

We note that the minimal gap is at the momentum M point in the Brillouin zone (see Fig. 8).

The estimated finite-size pairing gaps and single-particle gaps for sizes $L = 6, 9, \ldots, 18$ are shown in Fig. 9. We consider values of λ that lie deep within the K-IVC phase: $\lambda = 0.03$ for $\Delta = 0.75$, $\lambda = 0.035$ for $\Delta = 0.5$, and $\lambda = 0.043$ for $\Delta = 0.1$. For odd L (9 and 15), we select the nearest momentum around the M point to calculate Δ_{sp}. This explains the even-odd oscillations in the finite-size estimators (see Fig. 9).

Overall, the single-particle gap Δ_{sp} is larger than half of the pairing gap $\Delta_{SC}/2$ for all three values of Δ, thus indicating that the lowest charge excitation is a pair. The pairing energy is defined as $\Delta_{Pairing} = 2\Delta_{sp} - \Delta_{SC}$. Let us now consider only the even lattice sizes for which the single-particle gap shows little size effects. In this case, we observe that the pairing energy decreases as the easy-plane anisotropy grows. This is consistent with our understanding based on the meron picture: although the norm of the K-IVC U(1) order parameter (corresponding to the single-particle gap) has no significant dependence on the anisotropy, pairs of merons require less excitation energy as the anisotropy grows. This stems from our understanding that as the anisotropy grows the meron core becomes more energetically expensive.

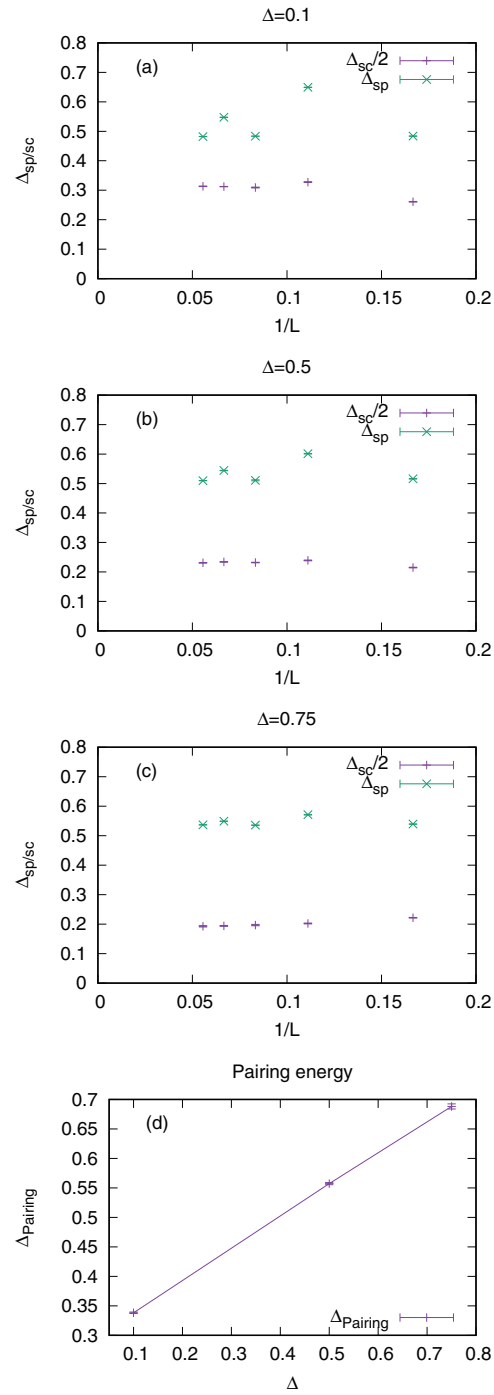

FIG. 9. Pairing gap and single-particle gap as functions of $1/L$ in the K-IVC state for three cases: (a) $\Delta = 0.1$, $\lambda = 0.043$; (b) $\Delta = 0.5$, $\lambda = 0.035$; and (c) $\Delta = 0.75$, $\lambda = 0.03$. The gap of preformed pairs $\Delta_{Pairing} \equiv 2\Delta_{sp} - \Delta_{SC}$ for $L = 18$ is shown in Fig. (d).

[1] M. Yankowitz, S. Chen, H. Polshyn, Y. Zhang, K. Watanabe, T. Taniguchi, D. Graf, A. F. Young, and C. R. Dean, Tuning superconductivity in twisted bilayer graphene, Science **363**, 1059 (2019).

[2] Y. Cao, V. Fatemi, A. Demir, S. Fang, S. L. Tomarken, J. Y. Luo, J. D. Sanchez-Yamagishi, K. Watanabe, T. Taniguchi, E. Kaxiras, R. C. Ashoori, and P. Jarillo-Herrero, Correlated insulator behaviour at half-filling in magic-angle graphene superlattices, Nature (London) **556**, 80 (2018).

[3] Y. Cao, V. Fatemi, S. Fang, K. Watanabe, T. Taniguchi, E. Kaxiras, and P. Jarillo-Herrero, Unconventional superconductivity in magic-angle graphene superlattices, Nature (London) **556**, 43 (2018).

[4] J. P. Hong, T. Soejima, and M. P. Zaletel, Detecting symmetry breaking in magic angle graphene using scanning tunneling microscopy, Phys. Rev. Lett. **129**, 147001 (2022).

[5] E. Khalaf, S. Chatterjee, N. Bultinck, M. P. Zaletel, and A. Vishwanath, Charged skyrmions and topological origin of superconductivity in magic-angle graphene, Sci. Adv. **7**, eabf5299 (2021).

[6] Y. H. Kwan, G. Wagner, N. Bultinck, S. H. Simon, and S. A. Parameswaran, Skyrmions in twisted bilayer graphene: Stability, pairing, and crystallization, Phys. Rev. X **12**, 031020 (2022).

[7] N. Bultinck, E. Khalaf, S. Liu, S. Chatterjee, A. Vishwanath, and M. P. Zaletel, Ground state and hidden symmetry of magic-angle graphene at even integer filling, Phys. Rev. X **10**, 031034 (2020).

[8] S. Chatterjee, M. Ippoliti, and M. P. Zaletel, Skyrmion superconductivity: Dmrg evidence for a topological route to superconductivity, Phys. Rev. B **106**, 035421 (2022).

[9] D. Hou, Y. Liu, T. Sato, W. Guo, F. F. Assaad, and Z. Wang, Bandwidth-controlled quantum phase transition between an easy-plane quantum spin Hall state and an *s*-wave superconductor, Phys. Rev. B **107**, 155107 (2023).

[10] T. Grover and T. Senthil, Topological spin Hall states, charged skyrmions, and superconductivity in two dimensions, Phys. Rev. Lett. **100**, 156804 (2008).

[11] Y. Liu, Z. Wang, T. Sato, M. Hohenadler, C. Wang, W. Guo, and F. F. Assaad, Superconductivity from the condensation of topological defects in a quantum spin-Hall insulator, Nat. Commun. **10**, 2658 (2019).

[12] Z. Wang, Y. Liu, T. Sato, M. Hohenadler, C. Wang, W. Guo, and F. F. Assaad, Doping-induced quantum spin Hall insulator to superconductor transition, Phys. Rev. Lett. **126**, 205701 (2021).

[13] C. L. Kane and E. J. Mele, Z_2 topological order and the quantum spin Hall effect, Phys. Rev. Lett. **95**, 146802 (2005).

[14] From now on, we identify the K-IVC state in continuum description of MATBG as the dynamically generated QSH state in our model, and keep the name of K-IVC throughout the text.

[15] F. F. Assaad, M. Bercx, F. Goth, A. Götz, J. S. Hofmann, E. Huffman, Z. Liu, F. P. Toldin, J. S. E. Portela, and J. Schwab, The ALF (Algorithms for Lattice Fermions) project release 2.0. Documentation for the auxiliary-field quantum Monte Carlo code, SciPost Phys. Codebases1 (2022).

[16] R. Blankenbecler, D. J. Scalapino, and R. L. Sugar, Monte carlo calculations of coupled boson-fermion systems, Phys. Rev. D **24**, 2278 (1981).

[17] S. R. White, D. J. Scalapino, R. L. Sugar, E. Y. Loh, J. E. Gubernatis, and R. T. Scalettar, Numerical study of the two-dimensional Hubbard model, Phys. Rev. B **40**, 506 (1989).

[18] F. Assaad and H. Evertz, World-line and determinantal quantum Monte Carlo methods for spins, phonons and electrons, in *Computational Many-Particle Physics*, Lecture Notes in Physics, edited by H. Fehske, R. Schneider, and A. Weiße (Springer, Berlin, 2008), Vol. 739, pp. 277–356.

[19] C. Wu and S.-C. Zhang, Sufficient condition for absence of the sign problem in the fermionic quantum Monte Carlo algorithm, Phys. Rev. B **71**, 155115 (2005).

[20] G. Sugiyama and S. E. Koonin, Auxiliary field Monte-Carlo for quantum many-body ground states, Ann. Phys. **168**, 1 (1986).

[21] S. Sorella, S. Baroni, R. Car, and M. Parrinello, A novel technique for the simulation of interacting fermion systems, Europhys. Lett. **8**, 663 (1989).

[22] For a finite-size calculation in the canonical ensemble, one may need a very large system to observe phase separation due to the energetics of the domain boundary.

[23] M. P. A. Fisher, P. B. Weichman, G. Grinstein, and D. S. Fisher, Boson localization and the superfluid-insulator transition, Phys. Rev. B **40**, 546 (1989).

[24] M. Hasenbusch, Monte Carlo study of an improved clock model in three dimensions, Phys. Rev. B **100**, 224517 (2019).

[25] R. Bistritzer and A. H. MacDonald, Moiré bands in twisted double-layer graphene, Proc. Natl. Acad. Sci. USA **108**, 12233 (2011).

[26] X. Zhang, G. Pan, Y. Zhang, J. Kang, and Z. Y. Meng, Momentum space quantum Monte Carlo on twisted bilayer graphene, Chin. Phys. Lett. **38**, 077305 (2021).

[27] J. S. Hofmann, E. Khalaf, A. Vishwanath, E. Berg, and J. Y. Lee, Fermionic Monte Carlo study of a realistic model of twisted bilayer graphene, Phys. Rev. X **12**, 011061 (2022).

[28] K. S. D. Beach, Identifying the maximum entropy method as a special limit of stochastic analytic continuation, arXiv:cond-mat/0403055.